Investigation of Ti 0.54 Al 0.46 /Ti 0.54 Al 0.46 N multilayer films deposited by reactive gas pulsing process by nano-indentation and electron energy-loss spectroscopy

Marie-Josée Pac, Yves Pinot, Sylvain Giljean, Christophe Rousselot, Patrick Delobelle, Corinne Bouillet, Marie-Hélène Tuillier

Investigation of $Ti_{0.54}Al_{0.46}/Ti_{0.54}Al_{0.46}N$ multilayer films deposited by reactive gas pulsing process by nano-indentation and electron energy-loss spectroscopy

M.-J. Pac[a*], Y. Pinot[a], S. Giljean[a], C. Rousselot[b], P. Delobelle[c], C. Ulhaq-Bouillet[d], and M.-H. Tuilier[a]

[a] Université de Haute Alsace, Laboratoire de Physique et Mécanique Textiles (EA 4365), F-68093 Mulhouse, France.

[b] Université de Franche-Comté, FEMTO-ST/MN2S (UMR CNRS 6174), F-25211 Montbéliard, France.

[c] Université de Franche-Comté, FEMTO-ST/DMA (UMR CNRS 6174), F-25030 Besançon, France

[d] Université de Strasbourg, Institut de Physique et Chimie des Matériaux de Strasbourg (UMR CNRS 7504), F-67087 Strasbourg, France

Abstract

Physical vapour deposition technology is well suited to the deposition of advanced TiAlN-based coatings. Among these thin films, multilayer systems consisting of stacked layers of metallic $Ti_{1-x}Al_x$ and nitride $Ti_{1-x}Al_xN$ with x around 0.5 are expected to have improved mechanical properties with respect to single nitride layers of the same composition. A set of $Ti_{0.54}Al_{0.46}/Ti_{0.54}Al_{0.46}N$ multilayer films with five different periods Λ (from 4 to 50 nm) were deposited using the Reactive Gas Pulsing Process (RGPP). This RGPP approach allows the deposition of TiAl-based alloy/nitride multilayer films by radio frequency reactive magnetron sputtering with a controlled pulsing flow rate of the nitrogen reactive gas. The coherent growth of the multilayer coatings, depending on the period, is checked by X-ray diffraction and the

[*]Corresponding author. Tel: +33 389337518
E-mail address: marie-jose.pac@uha.fr

mechanical properties are determined by Berkovich nano-indentation and friction experiments. A model to describe the dependence of the indentation modulus M and the hardness H_B on the penetration depth h, the period Λ, and the film thickness e_f is proposed. The indentation modulus of the multilayer films (M at h = 0 and for $e_f \sim 1900$ nm) is found to be in the range of 340 GPa < M < 525 GPa ≈ M($Ti_{0.54}Al_{0.46}N$). For a fixed penetration depth, M follows a Hall and Petch evolution as a function of the period ($4 \leq \Lambda \leq 50$ nm). The Berkovich hardness, 25 GPa < H_B < 50 GPa, also presents the same kind of evolution, and for Λ < 16 nm (at h = 0), $H_B > H_B$ ($Ti_{0.54}Al_{0.46}N$) = 33 GPa. Hence, a superlattice effect is clearly evidenced. Moreover, for the larger periods, the wear behaviour of these multilayered coatings seems to be dominated by the plastic deformation of the metallic layer. The multilayer coating of period Λ = 10 nm, which exhibits a diffraction pattern typical of superlattices and favourable mechanical properties, is more precisely investigated. Transmission electron microscopy confirms the main growth of the film along the [111] direction, and the evolution of the bonding of nitrogen in the direction normal to the rough interfaces between $Ti_{0.54}Al_{0.46}$ and $Ti_{0.54}Al_{0.46}N$ layers is specified by electron energy-loss near-edge spectroscopy. Nitride nano-grains are included in the metallic layer, which attests to the mixing of nitrogen into the layers. The structure of these nano-grains presents a progressive evolution into the layer and gradually acquires a TiN-like structure near the interface. For this Λ = 10 nm period, the indentation modulus and hardness for different penetration depths are weakly sensitive to the multilayer film thickness.

Keywords: TiAl-based alloy/nitride multilayer films, Reactive gas pulsing process, Nano-indentation, X-ray diffraction, Electron Energy-Loss Spectroscopy.

I. Introduction

Metal nitride coatings such as titanium and aluminium nitride films have attracted considerable interest because of their physical and chemical properties such as oxidation resistance and excellent mechanical performances due to their high hardness, toughness, and wear resistance [1]. They are extensively used in industry and particularly in machining applications as protective coatings of cutting tools [2]. $Ti_{1-x}Al_xN$ can be considered as a ternary nitride model system in which the crystallographic structure evolves from the face centered cubic (fcc) NaCl lattice for low Al contents to the hexagonal wurtzite-type (hcp) for high Al contents. Although AlN is poorly soluble in TiN, the reactive sputtering from a TiAl metallic target allows the deposition of coatings in which Al atoms are partially substituted for Ti [3,4]. The best mechanical properties are obtained when the maximum Al content is substituted for Ti in the fcc lattice [5,6]. For as-deposited coatings, which exhibit columnar microstructure, the indentation modulus M and the Berkovich hardness H_B values are strongly dependent on the composition of $Ti_{1-x}Al_xN$, and a transition occurs when both fcc and hcp phases grow in the film [3,7]. The best mechanical properties – high hardness and wear resistance – are observed for films whose Al content is around 50 at.% of the metallic part.

Various attempts to improve the performances of hard coatings have been carried out. One way consists in depositing TiAlN-based multilayer coatings in order to combine different properties. The large number of interfaces in multilayer films prepared by the Physical Vapour Deposition (PVD) technique ensures energy dissipation and improves the toughness and crack-propagation resistance [8]. Excellent cutting performances are obtained from multilayer coatings consisting of stacked layers of metallic and covalent hard materials. Vogli et al. have analysed the hardness and wear coefficient of PVD metal/ceramic Ti/TiAlN multilayers with different designs [9,10]. They found that a multilayer film with the thickest TiAlN layers has the highest hardness and

lowest wear coefficient. The mechanical performance of coatings based on TiAlN and either metallic Ti or Al interlayers has been studied [11]. The hardness and Young's modulus measured for multilayer films with Ti interlayers are of the same order of magnitude as those of TiAlN thin films, while these values are lower with Al interlayers. In some metallic nitride multilayer systems, Transmission Electron Microscopy (TEM) and Electron Energy-Loss Spectroscopy (EELS) have evidenced intermixing, despite a coherent growth of the superlattices [12,13]. Core level spectroscopies like extended X-ray absorption fine structure have proved useful to probe intermixing within low- or large-period multilayer films [14-16], but the EELS technique has the advantage of combining imaging and investigation of the local order at the nano-scale [17].

The present work focuses on the properties of alternating $Ti_{0.54}Al_{0.46}$ and $Ti_{0.54}Al_{0.46}N$ layers deposited by reactive magnetron sputtering. An Al content of 46 at.% was chosen because it corresponds to the composition of the ternary coating exhibiting the best mechanical performances [7,18]. A set of multilayer coatings with five different periods was elaborated using a Reactive Gas Pulsing Process (RGPP) [19]. This approach should allow the fabrication of TiAl-based alloy/nitride multilayer films by radio frequency (RF) reactive magnetron sputtering with a controlled pulsing flow rate of nitrogen reactive gas. The argon flow rate was kept constant during sputtering of a sintered TiAl alloy target while the nitrogen flow rate was periodically pulsed as a rectangular wave function during deposition. This RGPP approach has already been successfully used to deposit, from one metallic target (M) and one reactive gas, O_2, single systems like metal oxynitride films (TiON [20,21], FeON [22-24], TaON, NbON [25], ZrON [26], or SiON[27]) or metal/oxide multilayer films (Ti/TiO_2, W/WO_3, Ta/Ta_2O_5 [28-30]) by pulsing oxygen gas flow. One work has been devoted to the deposition of complex systems using the RGPP process with two targets (M1 and M2) and one reactive gas N_2 by pulsing nitrogen gas flow [31]. The deposition of nitride multilayers or alloy/nitride multilayer

films with a single alloy target (M1M2) and one reactive gas, N_2, has never been achieved using pulsed nitrogen flow until now. The main purpose of this work is to establish that this RGPP process using a single alloy target (TiAl) and one reactive gas, N_2, allows deposition of $Ti_{0.54}Al_{0.46}/Ti_{0.54}Al_{0.46}N$ multilayer coatings with different periods Λ and to characterize the structure and mechanical properties of as-deposited films. X-ray diffraction (XRD) and nano-indentation and friction tests were carried out on the set of films in order to investigate the influence of the multilayer period. Then, special attention was paid to the film with a period of 10 nm, which exhibits good mechanical properties. The influence of the film thickness on the hardness and indentation modulus was investigated and EELS was used to probe the local environment of nitrogen atoms within each of the two layers and thus to evaluate the degree of interdiffusion.

II. Experimental

2.1 Elaboration and multilayer design

Thin films were deposited onto silicon (100) wafer by RF magnetron sputtering in an Alliance Concept AC450 vacuum reactor. One sintered titanium/aluminium 66/33 at.% alloy target (purity 99.99%, 50 mm diameter, and 6 mm thickness) was RF sputtered at 13.56 MHz in an Ar or Ar + N_2 atmosphere. The distance between the target and the substrate was fixed at 60 mm and the temperature was kept at room temperature. The substrates and the TiAl target were cleaned before deposition. The substrates were etched in situ using argon ion bombardment in pure argon at 0.8 Pa with an applied RF bias voltage of 400 V during 15 min. The TiAl target was pre-sputtered in a pure argon atmosphere at 0.8 Pa for 15 min. The sputtering power applied was 80 W. All deposition was carried out with a constant argon flow rate of 3 sccm and a constant pumping speed of 10 $L.s^{-1}$. The nitrogen flow rate was pulsed with a variable period T ranging from 44 to 480 s. During this period, the nitrogen flow rate was modulated as a

rectangular wave function versus time (Table 1). The minimum and maximum nitrogen flow rates, Q_{min} and Q_{max}, were kept constant at Q_{min} = 0 sccm and Q_{max} = 5 sccm. Those conditions were chosen in order to alternate the reactive sputtering process between the alloy and compound sputtering mode, which corresponds to changing the total pressure between 0.52 Pa (alloy deposition) and 0.65 Pa (nitride deposition). The nitrogen injection time t_{on} and the nitrogen closing time t_{off} ($T = t_{on} + t_{off}$) were systematically changed for each multilayer film and calculated from the deposition rate of a single layer of alloy and nitride (Table 1). The expected period Λ for each multilayer film is defined as $\Lambda = \lambda_{TiAl} + \lambda_{TiAlN}$, with $\lambda_{TiAl} = \lambda_{TiAlN}$, where λ_{TiAl} and λ_{TiAlN} are the thicknesses of the alloy and nitride sub-layers, respectively. The deposition time was adjusted to obtain a total thickness of the film close to 2 µm (Table 1). For all samples, the first layer on the Si substrate is $Ti_{0.54}Al_{0.46}$ and the upper layer is $Ti_{0.54}Al_{0.46}N$. For Λ = 10 nm, films with different thicknesses ranging from 700 to 3200 nm were elaborated. $Ti_{0.54}Al_{0.46}$ and $Ti_{0.54}Al_{0.46}N$ single layers were also deposited to compare their properties with those of the $Ti_{0.54}Al_{0.46}/Ti_{0.54}Al_{0.46}N$ multilayer films with different periods. The element compositions were determined by energy-dispersive X-ray emission spectroscopy and wavelength-dispersive emission spectroscopy in a scanning electron microscope (SEM) under voltages of 5 and 10 kV after calibration.

Table 1: *Pulsed nitrogen parameters and characteristics of the multilayer films*

Pulsing period T (s)	t_{on} (s)	t_{off} (s)	$\lambda_{TiAl} = \lambda_{TiAlN}$ (nm)	Period Λ (nm)	Film thickness ef (nm)	Stacking number (ef/Λ)
480	378	102	25	50	2000	40
230	181	49	12	24	1800	75
160	123	37	8	16	1970	123
90	65	25	5	10	1790	179
44	30	14	2	4	1850	462

2.2 Analysis methods

The crystalline structure of the films was investigated by XRD using a Rigaku Smartlab (9 kW) diffractometer equipped with a Cu Kα1 source (λ = 1.54056 Å) and a Ge (220) two-bounce front monochromator. XRD patterns were recorded at room temperature in θ–2θ parallel mode in the range of 35–50°. The high-angle XRD resulting from diffraction of atomic planes in the superlattice is due to convolution of the crystalline structure of the layers with the modulation of the composition [32].

TEM measurements were performed on a Cs-corrected JEOL 2100F microscope, operating at 200 kV and equipped with an EELS Gatan Imaging Filter (GIF) spectrometer. The morphology and crystalline structure were studied by high-resolution Selected-Area Electron Diffraction (SAED). Scanning Transmission Electron Microscopy (STEM) imaging with a 0.15 nm probe was used for chemical determination of interfaces, and the GIF spectrometer fit with a collection angle set to 30 mrad and a dispersion of 0.2 eV energy channel was used to record Electron Energy-Loss Near-Edge Structure (ELNES) spectra. Different line scans on several interfaces were recorded on the cross-section, prepared by focused ion beam.

Nano-indentation tests were performed on the films using a CSM (now Anton Paar) instrument equipped with a UNHT (Ultra Nano-indentation Hardness Tester) head and a Berkovich tip whose radius is of the order of 100 ± 20 nm. For each film, the measurement sequence consisted in 6 indentations with a 50-µm space between them. The tests were conducted following the progressive multi-cycles procedure (CMC) in load control. Hence, for each indentation, eight loading (P_{max}) – unloading (90% of P_{max}) cycles were applied. P_{max} follows a quadratic progression such that P_{max} = 570, 720, 1180, 1960, 3020, 4420, 6110, and 8060 µN. For each cycle, the loading–unloading time was fixed at 30 × 2 = 60 s. However, as further shown, due

to its surface referencing system the UNHT head virtually eliminates the effect of the thermal drift and the different loops are perfectly closed and reversible.

Friction tests were performed using a CSM Instruments Micro-Combi-Tester with an alumina ball counterpart (1 mm diameter) under an applied load of 80 mN. The friction track was 1 mm long and 500 back and forth cycles were run for a total sliding distance of 1 m with a constant velocity fixed at 20 mm. min^{-1}. More details of the experimental parameters are explained in Ref. [18].

III. Effect of multilayer period on microstructural and mechanical properties of $Ti_{0.54}Al_{0.46}/Ti_{0.54}Al_{0.46}N$ films

3.1 X-ray Diffraction

The out-of-plane θ–2θ XRD patterns of $Ti_{0.54}Al_{0.46}N$ and $Ti_{0.54}Al_{0.46}$ single layers are presented in Fig. 1a. The nitride film $Ti_{0.54}Al_{0.46}N$ exhibits the typical pattern of the NaCl fcc crystal structure with [111] and [200] as the principal growth directions. The interplanar distances (Bragg's formula) are d_{111} = 2.43 Å and d_{200} = 2.11 Å, leading to the lattice parameters a_{111} = 4.21 ± 0.01 Å and a_{200} = 4.23 ± 0.01 Å. The slight difference in the lattice parameters derived from the 200 and 111 peak positions has already been discussed in Ref. [33]. The bump observed near 2θ ~ 38.5° is a $Ti_{0.54}Al_{0.46}$ reflection due to the 45-nm-thick $Ti_{0.54}Al_{0.46}$ underlayer first deposited on the substrate to improve the coating adhesion.

The metallic layer $Ti_{0.54}Al_{0.46}$ shows only one crystalline orientation along the [111] direction of a tetragonal structure. The deduced value of the interplanar spacing is 2.32 ± 0.01 Å. For an ideal binary alloy, the corresponding a and c relaxed lattice parameters would be 4.00 Å and 4.08 Å respectively.

Figure 1b presents the diffraction patterns performed on the set of $Ti_{0.54}Al_{0.46}$ / $Ti_{0.54}Al_{0.46}N$ multilayers with Λ ranging from 4 to 50 nm. XRD data of the multilayer of period Λ = 4 nm show TiAl and (TiAl)N crystallites growing along the (200) and (111) orientations of each lattice respectively. The most intense peaks are assigned to (TiAl)N grains and the broadness of all the peaks indicates some small cubic (TiAl)N and TiAl tetragonal domains. For ultra-thin period films, the typical interferences of a multilayer system are not observed because of the interdiffusion between the layers [34]. The interplanar distances calculated from the 111 peaks, d_{TiAl} = 2.34 ± 0.02 Å and d_{TiAlN} = 2.41 ± 0.02 Å, are close to the values obtained for the reference single layers.

The XRD patterns of the 10- and 16-nm-period multilayers exhibit a prominent reflection (θ_0) flanked by satellite reflections (θ_i) characteristic of the superlattice. The growth direction is along the <111> planes. First- and second-order satellite reflections are observed around the corresponding Bragg peak. For a period of Λ = 10 nm, the multilayer film presents a well-defined pattern indicating a good texturation around the [111] direction. In contrast, for a periodicity of 16 nm, an additional broad peak is observed at 2θ = 42.40° corresponding to the [200] axis of the NaCl-type crystal, which reveals a poorer organization in the film. The average interplanar d spacing values of the multilayer films are between those of $Ti_{0.54}Al_{0.46}$ and $Ti_{0.54}Al_{0.46}N$ single layers (Eq. (1)) and the period of the superlattice can be calculated using Eq. (2).

$$d = \frac{\lambda}{2\sin\theta_0} \qquad \text{Eq. (1)}$$

$$\Lambda = \left|\frac{i\lambda}{2(\sin\theta_i - \sin\theta_0)}\right| \qquad \text{Eq. (2)}$$

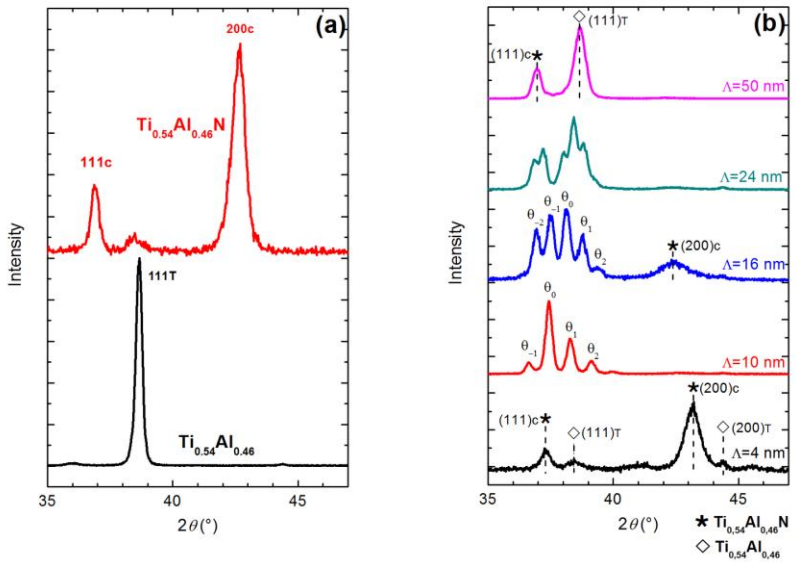

Fig. 1: XRD patterns of (a) single layer $Ti_{0.54}Al_{0.46}N$ coating and $Ti_{0.54}Al_{0.46}$ coating; (b) $Ti_{0.54}Al_{0.46}/Ti_{0.54}Al_{0.46}N$ multilayer coatings with different Λ periods (4, 10, 16, 24, and 50 nm).

The values calculated from XRD data show good agreement with the ones expected during the deposition process (Table 2).

Table 2: Superlattice periods and interplanar distances (Eq. (1)) calculated from XRD data for the two $Ti_{0.54}Al_{0.46}$ / $Ti_{0.54}Al_{0.46}N$ multilayer films, which present a well-definied pattern (Fig.1)

$\Lambda_{expected}$ (nm)	$\Lambda_{measured}$ (nm)	d (Å)
10	11.0 ± 0.1	2.40 ± 0.02
16	14.9 ± 0.1	2.36 ± 0.02

For the largest periods of the multilayer films (Fig. 1b), the superstructure is damped and completely disappears. Two dissociated peaks assigned to the (111) orientation of the cubic $Ti_{0.54}Al_{0.46}N$ and tetragonal $Ti_{0.54}Al_{0.46}$ lattice are observed for the 50-nm-period film.

3.2 Mechanical properties

3.2.1 Nano-indentation results

Among the numerous results, Fig. 2 shows three complete indentation curves, load P versus the penetration depth h (8 cycles) for Λ = 4, 16, and 50 nm. The inset represents a magnified view of the two first cycles, which correspond to relatively low penetration depths. The loops are perfectly reversible and closed. Hence, from the unloading path of each cycle and according to the Oliver and Pharr relations [35], the indentation modulus M_{meas} and the Berkovich hardness H_{Bmeas} can be determined. Note that these two quantities depend on the [hkl] direction of the domain growth [7,36].

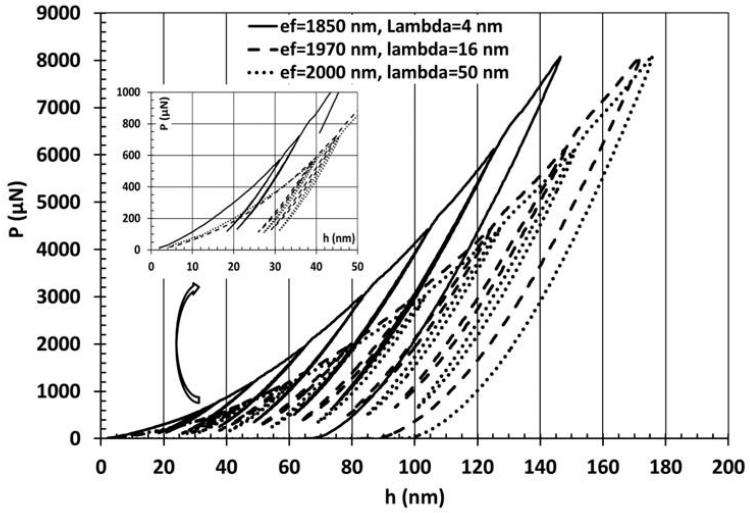

Fig. 2: Exemple of three indention curves P = f(h) for Λ = 4, 16, and 50 nm

i) Indentation modulus as a function of the period Λ for a given thickness, $e_f \sim 1.9$ µm

Figure 3a represents, for each film, the mean measured values of the indentation modulus M_{meas} versus the indentation depth h. As the indentation modulus of the Si substrate ($M_s = M(Si) =$ 173 GPa) is lower than those of the deposited films, due to the substrate effect, the measured moduli decrease continuously with the indentation depth. Moreover, whatever the penetration

depth, the indentation moduli of the multilayers clearly decrease with the period Λ and the curves are located between those of TiAlN (upper bound) and TiAl (lower bound). The true indentation modulus M (homogenized equivalent modulus) of the films can be determined by extrapolating the measured values to h = 0. Among the numerous analytical expressions, in order to take into account the substrate and the multilayer structure effects [37-42], a modified version of the King's model [39] was used. Hence, the measured indentation modulus M_{meas} is given by:

$$M_{meas} = \left[\frac{1}{M} + \left(\frac{1}{M_S} - \frac{1}{M}\right)\exp - \left(\frac{\alpha_0 e_f}{\sqrt{A_C}}\right)^n\right]^{-1} \quad \text{Eq. (3a)}$$

where A_c is the projected contact area $A_C = 24.56h_c^2 + \sum_0^7 a_n\, h_c^{1/2^n}$

and α_0 is a parameter that depends on the shape of the projected contact area. For a triangular contact like a Berkovich indenter,

$$\alpha_0 \approx \frac{1}{2} + \frac{3}{4}\left(\frac{\sqrt{A_C}}{e_f}\right)^{1/2} \quad \text{Eq. (3b)}$$

M and M_s are the indentation moduli of the coating and the substrate, respectively. The new exponent n depends on the deformation mode and controls the curvature of the M_{meas} = f(h) curves (Fig. 3a). n = 1 corresponds to the original version of King's model. Note that, when the argument of the exponential term of Eq. (3a) is small, $\exp - \left(\frac{\alpha_0 e_f}{\sqrt{A_C}}\right)^n \approx 1/(1 + \left(\alpha_0 e_f/\sqrt{A_C}\right)^n) \approx 1/(1 + \alpha_0(e_f/h)^n)$, which is an expression often used in the literature [42]. For the reference films made in a single layer, $Ti_{0.54}Al_{0.46}N$ and $Ti_{0.54}Al_{0.46}$, the model predictions with M_s = M(Si) = 173 GPa and n = 0.4 (the best fit) are plotted in Fig. 3a. Hence, $M_{<200>c}$ ($Ti_{0.54}Al_{0.46}N$) = 512 ± 26 GPa and $M_{<111>T}$ ($Ti_{0.54}Al_{0.46}$) = 212 ± 11 GPa. Taking the Poisson's coefficient as ν = 0.25, these two values are in a fairly good agreement

with the values of the Young's modulus E reported in the literature, that is, $M = E/(1 - \nu^2)$ = 394 GPa [3], 460 GPa [7], 618 GPa [43], and 630 GPa [44] for the $Ti_{1-x}Al_xN$ with the Al content, x, close to 0.5 and 220 to 250 GPa for thin TiAl films [45]. For the multilayer films, the definition of M_s in Eq. (3a) is not obvious as the elastic field crosses the stacking of the different layers. Thus, M_s is certainly a combination of the indentation moduli of the softest materials, M(Si) = 173 GPa and $M(Ti_{0.54}Al_{0.46})$ = 212 GPa. As previously, taking n = 0.4, the best fits were obtained with M_s = 130 GPa. Note that this value is close to the one calculated with the following relation:

$$M_s = \left(\frac{1}{M(Si)} + \frac{1}{M_H}\right)^{-1} = 130.4 \text{ GPa} \text{ with } M_H = M(TiAl)\left(\frac{\lambda_{TiAl}}{\Lambda} + \frac{\Lambda}{\lambda_{TiAl}}\right) = 530 \text{ GPa} \quad \text{Eq. (4)}$$

and $\lambda_{TiAl}/\Lambda = 0.5$ (since the elaboration conditions are $\Lambda = \lambda_{TiAl} + \lambda_{TiAlN}$ with $\lambda_{TiAl} = \lambda_{TiAlN}$).

In this equation, the indentation modulus M(Si) is associated with an equivalent modulus M_H in a serial manner and M_H is a parallel association of the two moduli $\lambda_{TiAl}M(TiAl)/\Lambda$ and $\Lambda M(TiAl)/\lambda_{TiAl}$. The M_H value is also close to $M(Ti_{0.54}Al_{0.46}N)$ = 512 GPa. In conclusion, the definition of M_s (Eq. (3a)) in the case of multilayered coatings composed of hard and soft layers deposited on a softer substrate is not obvious and needs a numerical analysis.

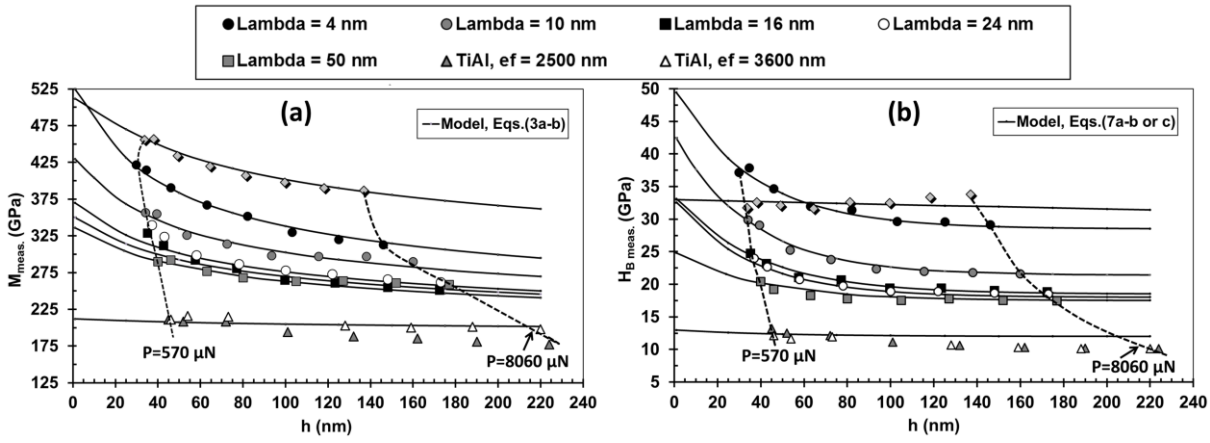

Fig. 3: Evolution of the (a) indentation modulus M and (b) Berkovich hardness H_B as a function of the penetration depth h. Experiments and modelling.

As shown in Fig. 4a, where the indentation modulus values M at h = 0 are plotted as a function of $1/\sqrt{\Lambda}$, a Hall and Petch evolution type can be evidenced. Hence, the period is substituted for grain size when characterizing the mechanical properties of these multilayers [32]. This can be modelled as:

$$M = M_0\left(1 + \sqrt{\frac{\Lambda_{0M}}{\Lambda}}\right) \qquad \text{Eq. (5)}$$

with M_0 = 260 GPa and Λ_{0M} = 4.1 nm. The value for Λ = 16 nm is slightly too low, which can be partially explained by a poorer organization in the multilayer, as observed on the XRD pattern. For Λ = 4 nm, the indentation modulus value, M = 530 $\pm$ 26 GPa, is very close to that of the $Ti_{0.54}Al_{0.46}N$ layer: $M_{<200>c}(Ti_{0.54}Al_{0.46}N)$ = 512 $\pm$ 26 GPa, which agrees with the XRD pattern (Fig. 1). Hence, from an elastic point of view and at h = 0, this coating behaves as a TiAlN film, but due to the presence of the TiAl layers, the decrease with indentation depth is more pronounced (Fig. 3a), which corroborates the M_s value given in the relation expressed by Eq. (4). A possible superlattice effect should be expected for multilayer films with Λ < 4 nm, that is, $M(\Lambda < 4\text{ nm}) > M(Ti_{0.54}Al_{0.46}N)$. The predictions for h = 40, 80, 120, and 160 nm and h = e_f using the model composed of Eqs. (3a,b) and (5) with n = 0.4 and M_s = 130 GPa are reported in Fig. 4a. They are in good agreement with the experimental measurements and, as expected for h = e_f, the M values are close to that of M(Si).

As far as the scattering of the measures is concerned, the standard deviation $\Delta M/M_{mean}$ is related to the dimensionless ratio (R_{ms}/h) [46,47] by the following relation:

$$\frac{\Delta M}{M_{mean}} = \delta\left(\frac{R_{ms}}{h}\right)^m \quad \text{for } h > 25\text{ nm} \qquad \text{Eq. (6)}$$

with $\delta = 0.35 \pm 0.1$ and m = 0.64. The R_{ms} roughness (root mean square) of the films was measured with an atomic force microscope in a non-contact mode. R_{ms} increases from about 2 nm for Λ = 4 nm to about 4.5 nm for Λ = 50 nm and is about 1.4 nm for a TiAlN single layer. Experimentally, for h = 40 nm, in the vicinity of the first cycles, 3.8% (Λ = 4 nm) < $\Delta M/M_{mean}$ < 6.5% (Λ = 50 nm). Of course, the scattering greatly decreases with the penetration depth and at h = 160 nm, $\Delta M/M_{mean}$ is in the range 1.4 to 2%. Thanks to the fit of the limit curves given by the experimental scattering, $\Delta M/M_{mean}$ at h = 0 was estimated to be 5%.

In conclusion, for $e_f \sim 1.9$ µm, knowing M(TiAlN) = 512 GPa, M(TiAl) = 212 GPa, n = 0.4, and Λ_{0M} = 4.1 nm, the complete model describing the evolution of the indentation moduli of the $Ti_{0.54}Al_{0.46}/Ti_{0.54}Al_{0.46}N$ films as a function of the multilayer period Λ and depth h is composed of Eqs. (3a,b), (4), and (5).

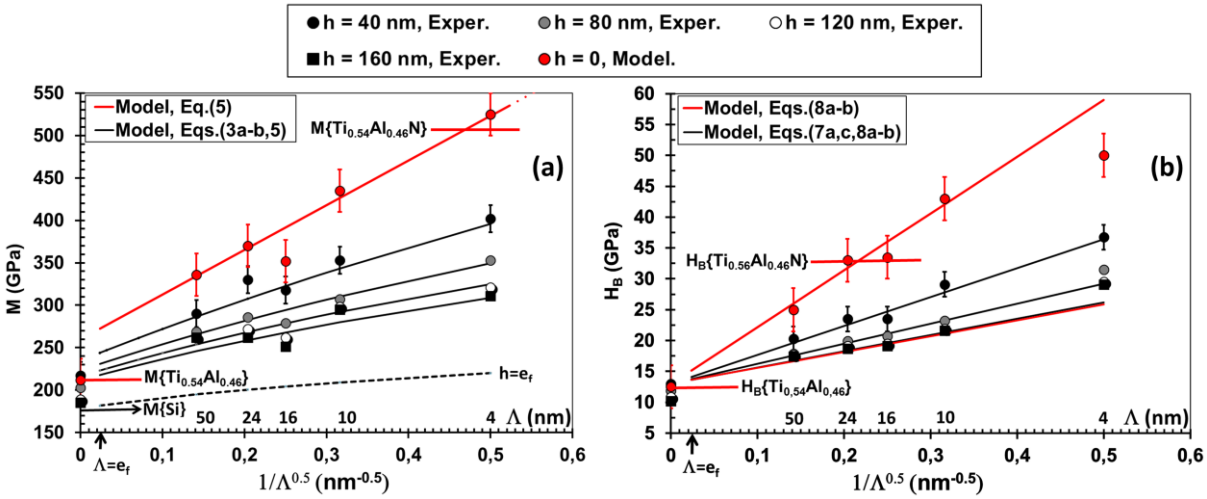

Fig. 4: Evolution of the (a) indentation modulus M and (b) Berkovich hardness H_B versus $1/\sqrt{\Lambda}$ for h = 0, 40, 80, 120, and 160 nm and e_f = 1900 nm. Experiments and modelling.

ii) Berkovich hardness as a function of the period Λ for a given thickness, $e_f \sim 1.9$ µm

Figure 3b shows, for all of the films, the measured Berkovich hardness H_{Bmeas} as a function of the indentation depth h. As for the film indentation modulus, the hardness decreases with the

penetration depth and the period Λ, which has very often been reported in the literature for different kinds of multilayers [48-50]. However, for TiAlN and TiAl films, the hardness is quasi-independent of the indentation depth. The maximum relative depth, h/e_f, is about 5% and 6–8% for the nitride and metallic films, respectively. These values are relatively small and consequently the plastic field seems to be confined in the film and does not reach the Si substrate. Hence, for the multilayer films, the decrease in hardness is linked more to a film structure effect than to a substrate effect. This point will be further discussed when the dependence of the hardness on the film thickness will be described. To quantitatively take this decrease into account and to determine the hardness H_B at h = 0, Bhattacharya and Nix's [51] relation for hard film on a softer substrate was considered. Thus:

$$H_{Bmeas} = H_{B\infty} + (H_B - H_{B\infty}) \exp(-\beta \frac{h}{e_f}) \quad \text{Eq. (7a)}$$

where $H_{B\infty} = H_s = H(Si) = 12$ GPa for the single layers TiAl and TiAlN and, as for the indentation modulus, has to be estimated from the experimental curves in the multilayer cases. In Bhattacharya and Nix's model,

$$\beta = \frac{H_B}{H_S} \frac{\sigma_S}{\sigma_f} \sqrt{\frac{M_S}{M}} \quad \text{Eq. (7b)}$$

σ_s and σ_f are the yield strengths of the substrate and the film, respectively. $\beta \approx 1.2$ for TiAlN [7] and the same value was considered for the TiAl film. For the multilayers, the relation expressed by Eq. (7b) is null and β has to be determined:

$$\beta = C^{te} \quad \text{Eq. (7c)}$$

As shown in Fig. 3b, the experimental tendencies are fairly well described by the relations expressed by Eqs. (7a,b) with $\beta = 1.2$ and $H_{B\infty} = H(Si)$ for the single layers TiAl and TiAlN and $\beta = 51$ and $H_{B\infty} = H_B(h/e_f \sim 10\%)$ (when the hardness becomes quasi-independent of the

penetration depth) for the multilayers. The hardness values at h = 0, $H_{B<200>c}$ = 33.0 $\pm$ 2.7 GPa and $H_{B<111>T}$ = 13.0 $\pm$ 1.3 GPa for the $Ti_{0.54}Al_{0.46}N$ and the $Ti_{0.54}Al_{0.46}$ films, respectively, are in good agreement with those reported in the literature [2,6,7,43,44,50]. The very different values of the parameter β indicate that the deformation mechanisms and the structure effects during the indentation of the single and multilayer films are very different. As shown in Fig. 4b, the hardness H_B at h = 0 and the hardness $H_{B\infty}$ at h ~ 200 nm follow a Hall and Petch evolution. Thus:

$$H_B = H_0\left(1 + \sqrt{\frac{\Lambda_{0H}}{\Lambda}}\right) \quad \text{(Eq. 8a)}$$

$$H_{B\infty} = H_0\left(1 + \sqrt{\frac{\Lambda_{\infty H}}{\Lambda}}\right) \quad \text{(Eq. 8b)}$$

with H_0 = 13 GPa ~ $H_B(Ti_{0.54}Al_{0.46})$ ~ $H_B(Si)$, Λ_{0H} = 50 nm, and $\Lambda_{\infty H}$ = 3.9 nm. The breakdown of the Hall and Petch behaviour at very small periods (the hardness increases with increases in the period) [48-50] has not been observed in this study. In Fig. 4b, it can be observed that at h = 0, for Λ = 4, 10, and 16 nm, the multilayers exhibit a superlattice effect as H_B > $H_B(Ti_{0.54}Al_{0.46}N)$. The results given by the model composed of Eqs. (7a,c) and (8a,b) are in fairly good agreement with the experimental ones. Moreover, at h = 0, the hardnesses of all the multilayer films, 25 $\pm$ 2 < H_B < 50 $\pm$ 4 GPa, are greater than (or of the order of) the one given by the mixture rule, H_B = 23 GPa.

As far as the relative scattering $\Delta H_B/H_{Bmean}$ is concerned, the experimental values at h ~ 40 nm are such that 5.6% (Λ = 4 nm) < $\Delta H_B/H_{Bmean}$ < 8.3% (Λ = 50 nm). Following the same procedure as the one proposed for the indentation modulus, the mean scattering at h = 0 was estimated to be 8%.

iii) Indentation modulus and hardness as a function of the film thicknesses

To study the dependence of the indentation modulus and the hardness on the coating thicknesses, films with the same period of Λ = 10 nm and different thicknesses, e_f = 700, 1230, 1790 (sample of above sections (i) and (ii)), 2460, and 3200 nm, were elaborated. The same indentation procedure as described above was applied to these films and the results are reported in Figs. 5a and 5b. Surprisingly, the responses are fairly close to each other, particularly for the hardness, showing that the indentation modulus and the hardness are weakly dependent on the film thickness, at least for h/e_f < 10% and 700 < e_f < 3200 nm. Hence, the decrease of the measured mechanical properties with indentation depth is mainly linked to a multilayer structure effect and in a smaller proportion to a substrate effect. This is particularly true for the hardness, the plastic deformation field being principally confined to the multilayer stacking. Equations (3a,b) and (7a,b) are not appropriate for quantitatively taking into account these two effects. The argument of the exponential functions in Eqs. (3a) and (7a) should be modified and the simplest way to do this is to write $\alpha = \alpha_0 f(e_f)$ and $\beta = \beta_0 g(e_f)$, where f and g are two functions of the film thickness.

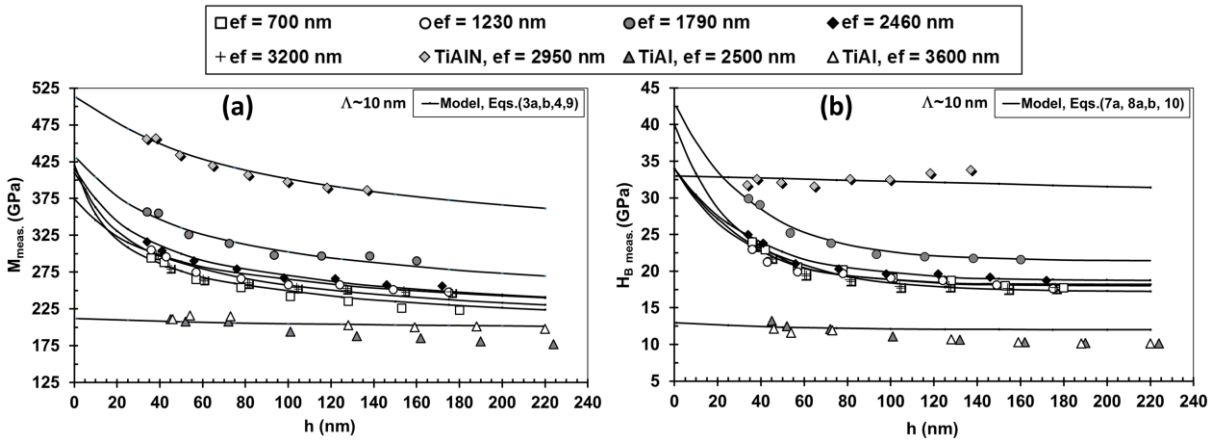

Fig. 5: Evolution of the (a) indentation modulus M and (b) Berkovich hardness H_B versus the indentation depth for different film thicknesses and Λ = 10 nm. Experiments and modelling.

Concerning the indentation modulus, as mentioned above, M and α were determined from the fit of the experimental curves with M_s = 130 GPa and n = 0.4. For e_f lower than 1790 nm, a good representation was obtained with $\alpha = \alpha_0$ (Eq. (3a)), but for e_f greater than 1790 nm, α is a decreasing function of the film thickness (Fig. 5a). To quantitatively take into account this evolution, Eq. (9) is proposed:

$$\alpha = \alpha_0\left(1 - \tanh < \frac{e_f}{e_{f0}} - 1 >^n\right) \qquad \text{Eq. (9)}$$

where <.> are the McCawley brackets [<x> = xH(x) with H(x) the Heaviside function], e_{f0} = 2000 nm and n = 0.4. Hence, for $e_f < e_{f0}$, $\alpha = \alpha_0$, and for $e_f > e_{f0}$, α decreases with the film thickness. The results given by the complete model expressed by Eqs. (3a,b) (α_0 is substituted by α), (4), and (9) are represented in Fig. 5a. Figure 6a represents, for different indentation depths, the evolutions of the indentation modulus as a function of the films' thicknesses. Thus, for h = 0, M is quasi-independent of e_f and the value is M = 410 $\pm$ 21 GPa, and for h = e_f, as expected, the indentation modulus is slightly higher to the M(Si) value. Two domains are clearly evidenced. For $e_f < 2000$ nm, the substrate effect with M_s = 130 GPa essentially controls the decrease with penetration depth, and in the opposite case the substrate and the bilayer structure effects operate simultaneously.

Concerning the hardness, the same identification procedure was performed: H_B at h = 0 and β were determined from the fit of the experimental curves (Fig. 5b). As mentioned above, $H_{B\infty}$ = H_B at h ~ 200 nm, when the hardness becomes quasi-independent of the penetration depth. β presents an increasing linear dependence on the film thickness and consequently the following relation is proposed:

$$\beta = \beta_0\left(1 + \frac{e_f}{e^*_{f0}}\right) \quad \text{with: } \beta_0 = 9.4 \text{ and } e^*_{f0} = 404 \text{ nm} \qquad \text{Eq. (10)}$$

Note that for e_f = 1790 nm, β = 51, as mentioned above (Section 3.2.1,ii).

So, Eq. (7a) is rewritten as:

$$H_{Bmeas} = H_{B\infty} + (H_B - H_{B\infty}) \exp(-\beta_0 \left(\frac{1}{e_f} + \frac{1}{e^*_{f0}}\right) h) \qquad \text{Eq. (11)}$$

Hence, for very large thickness, the hardness becomes independent of the film thickness, while in the opposite case of very small thickness, the substrate effect is dominant. In the present case of intermediate thicknesses, the two dependences are simultaneously active. The model is composed of Eqs. (7a) or (11) and (10) and the results are drawn in Fig. 5b. As for the indentation modulus, Fig. 6b reports the dependence of the hardness on the film thickness for different indentation depths. At h = 0, H_B is approximately independent of the thickness, H_B = 38 ± 3 GPa > $H_B(Ti_{0.54}Al_{0.46}N)$ = 33.0 ± 2.7 GPa, and a superlattice effect can be mentioned whatever the thicknesses. $H_{B\infty}$ can be considered as approximately constant and equal to $H_{B\infty}$ = 18.7 ± 1.6 GPa (Fig. 6b). However, the high values of H_B = 42.5 GPa and $H_{B\infty}$ = 21 GPa for e_f = 1790 nm are certainly related to the very well-defined multilayered texture around the [111] direction observed in the XRD pattern.

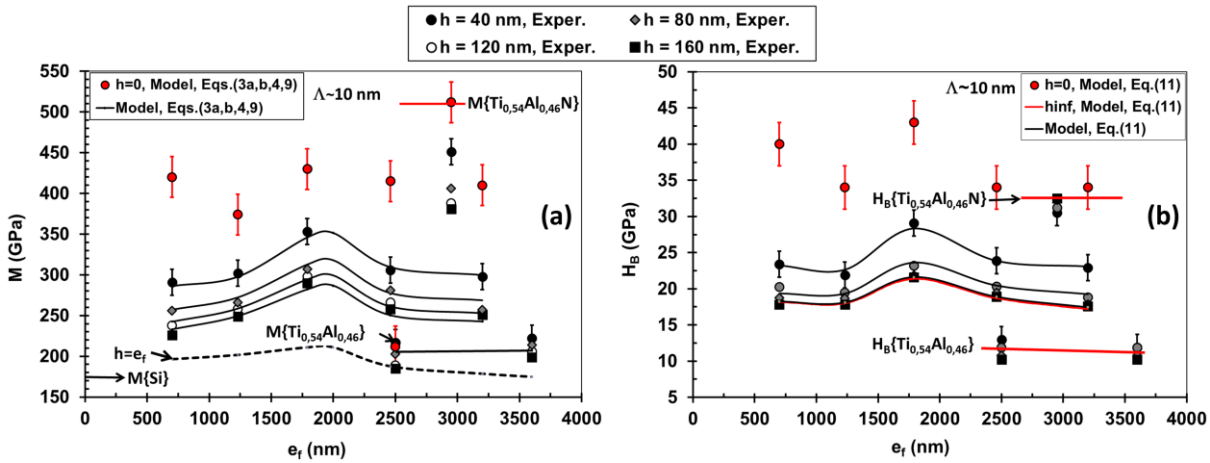

Fig. 6: (a) Indentation modulus M and (b) Berkovich hardness H_B as a function of the film thicknesses for Λ = 10 nm. Experiments and modelling.

3.2.2 Friction tests

Figure 7 shows the evolution, as a function of the period Λ, of the wear volume loss measured at the end of the friction tests performed on the same specimens. The volume is an increasing function of the period and is always greater than that obtained on a $Ti_{0.54}Al_{0.46}N$ single layer. The multilayer coating of Λ = 10 nm exhibits the smallest wear volume loss. The volume loss is inversely proportional to the load P_y (P_y α H^3/M^2) required to initiate plastic deformation [52]. Hence, the plastic deformation factor R = (M^2/H_B^3) was calculated for different indentation depths and reported as a function of the period in Fig. 7. For the maximum indentation penetration h = 160 nm, R and the wear volume loss approximately follow the same evolution. The R factor calculated from the above M and H_B models is also reported in Fig. 7. A transition occurs for films with periods close to 15–20 nm. Below this threshold, the wear volume loss is weak. In the opposite case, the volume greatly increases for higher periods, as established by the model prediction.

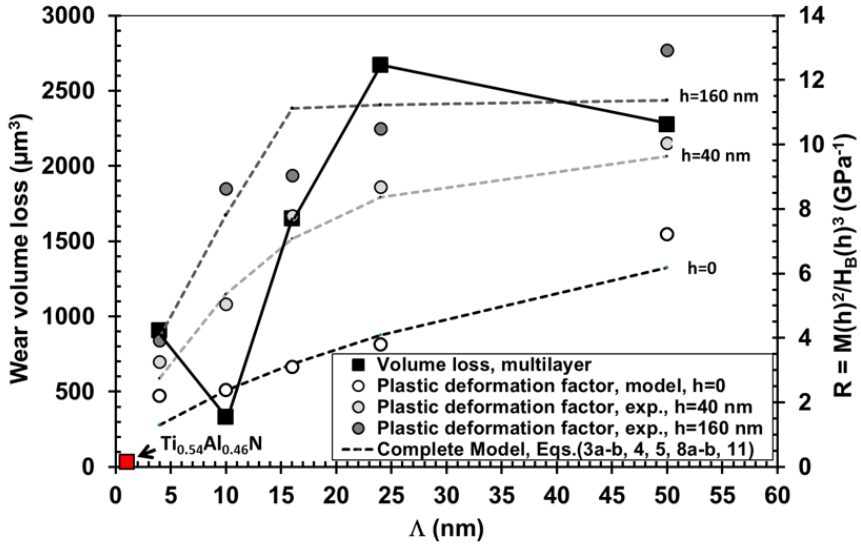

Fig. 7: Wear volume loss and plastic deformation factor R = (M^2/H_B^3) as a function of the period Λ. Experiments and model for the evaluation of the R factor.

IV. Transmission electron microscopy (TEM) and electron energy-loss spectroscopy (EELS) of the 10-nm-period $Ti_{0.54}Al_{0.46}/Ti_{0.54}Al_{0.46}N$ film

As shown above, the sample with a period of Λ = 10 nm presents a well-defined diffraction pattern and good mechanical properties: a high indentation modulus (~ 430 GPa), a superlattice effect on the hardness (~ 42.5 GPa), and a small wear volume loss. For these reasons, this sample was chosen for TEM and EELS investigations.

The cross-sectional image (Fig. 8a) shows the stacking up of dark $Ti_{0.54}Al_{0.46}$ and light $Ti_{0.54}Al_{0.46}N$ layers. In Fig. 9a, the SAED pattern performed on the cross-section shows the growth of TiAl/TiAlN domains along the [111] direction, represented by the red line. The yellow spots correspond to TiAlN domains oriented along the [200] (line 1), [111] (line 2), and [220] (line 3) directions, while the pink ones correspond to the TiAl domains oriented along the [111] (line 1), and [110] (line 2) directions. In Fig. 9b, the enlargement of the [111] spot along the growth direction shows interferences typical of a multilayer system. The corresponding intensity profile (Fig. 9c) is similar to the X-ray diffraction pattern (Fig. 1b).

The EELS spectra were recorded along the 16-nm-long red line every 0.3 nm in Fig. 8a. Some of them are plotted as a function of the spot position in Fig. 8b. The spectral region covers the N K-edge and the Ti L_2-L_3 edges. The more striking feature is that the N K-edge intensity decreases without cancelling out in the middle of the metallic $Ti_{0.54}Al_{0.46}$ layer. One can assume that intermixing occurs at the interfaces, as observed in previous works on PVD multilayers [14,15]. So, it is worth looking closely at the nitrogen bonding within the two components of the multilayer.

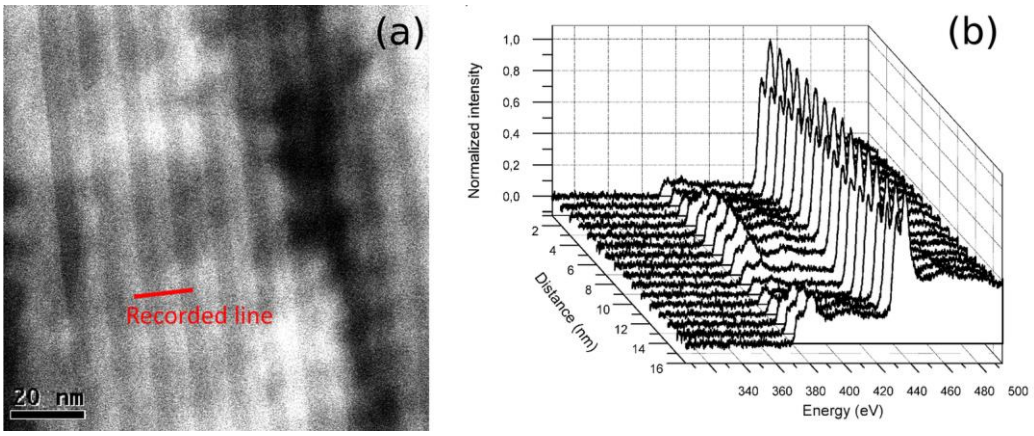

Fig. 8: (a) Bright-field STEM image of the cross-section of $Ti_{0.54}Al_{0.46}/Ti_{0.54}Al_{0.46}N$ multilayer film (Λ = 10 nm); (b) EELS spectra recorded along the red line in (a).

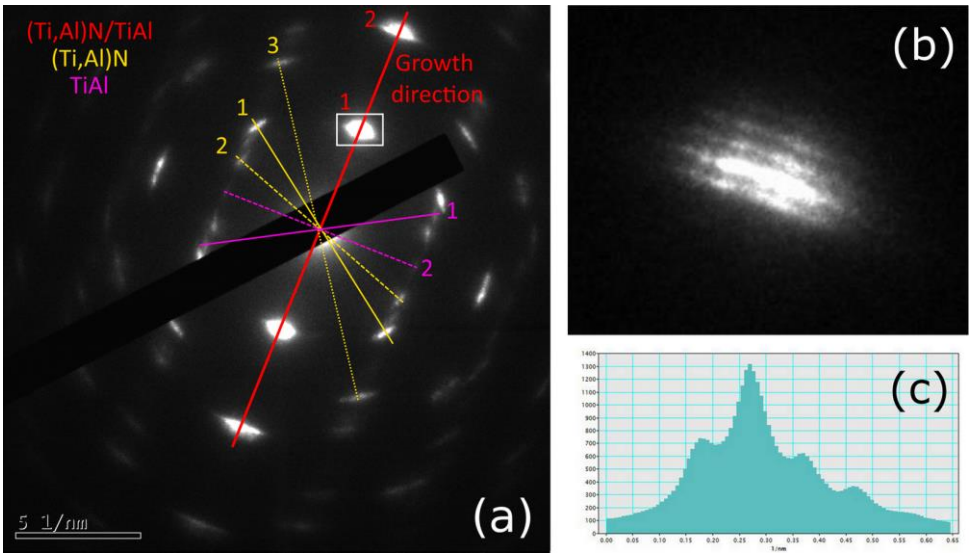

Fig. 9: (a) SAED pattern of $Ti_{0.54}Al_{0.46}/Ti_{0.54}Al_{0.46}N$ multilayer film (Λ = 10 nm); (b) enlargement of the spot along the [111] growth direction [rectangle drawn in (a)]; and (c) corresponding intensity profile.

ELNES spectra of standard $Ti_{1-x}Al_xN$ films prepared in roughly the same deposition conditions as the multilayer, $Ti_{0.54}Al_{0.46}N$, TiN and Al-rich $Ti_{0.14}Al_{0.86}N$ [18], are presented together with the spectra recorded at the centre of each of the metallic and nitride layers of the multilayer in Figs. 10a and 10b respectively. The pink line in Fig. 10b represents an average of eighteen

spectra recorded at either side of the middle of the $Ti_{0.54}Al_{0.46}N$ layer while the blue one is built from six spectra recorded at either side of the middle of the $Ti_{0.54}Al_{0.46}$ layer.

The spectra of Ti-rich films, $Ti_{0.54}Al_{0.46}N$, and pure rock salt TiN have their onset at about 396 eV and present a large feature centred at about 400 eV, assigned to the transition of 1s electrons towards unoccupied N 2p states. In cubic (fcc) TiN, N atoms are six-fold coordinated to Ti atoms and the interaction between nitrogen 2p orbitals and Ti 3d electrons leads to unoccupied hybridized states. The spectra of Al-rich films such as $Ti_{0.14}Al_{0.86}N$ film (dashed green line in Fig. 10a) have their onset shifted by about 4 eV towards the high energies [53] with respect to Ti-rich films and show the typical triple-peaked structure of w-AlN, which is also shifted with respect to the first bump (H) observed for Ti-rich films. These observations are in fairly good agreement with N K-edge X-ray Absorption Near Edge Structure (XANES) spectra of $Ti_{1-x}Al_xN$ films with progressive Al incorporation reported by Gago et al. [54,55]. For an easy comparison of our ELNES spectra with those XANES experiments, we used the same labels as in [55]: H for the first bump of Ti-rich films and I, J, and K for the three-peaked structure observed in Al-rich films. It has been well reproduced by DFT calculations [56] and is obviously related to the contribution of N sites surrounded by four metal atoms in wurtzite arrangements [18]. The presence of a shoulder at the energy of the H structure in the $Ti_{0.14}Al_{0.86}N$ spectrum, which is missing in w-AlN, has been assigned to the presence of six-fold-coordinated nitrogen out of the hcp columns of Al-rich nitrides [15]. The intensity of the H structure decreases with increasing Al content and is a fingerprint of the presence of less and less cubic-like nano-grains in the film. On the other hand, the second bump of $Ti_{0.54}Al_{0.46}N$ is shifted by about 2 eV towards the high energies with respect to the J peak observed for the $Ti_{0.14}Al_{0.86}N$ film.

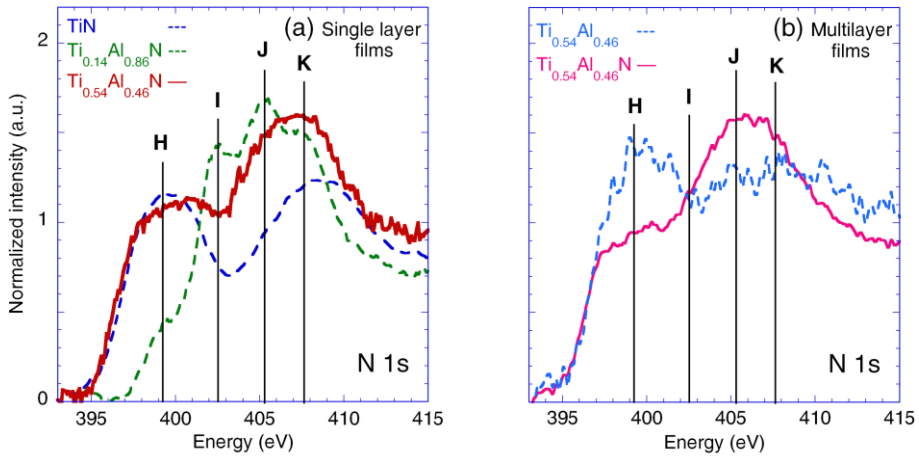

Fig. 10: N 1s ELNES spectra taken across (a) $Ti_{1-x}Al_xN$ film; (b) $Ti_{0.54}Al_{0.46}$ /$Ti_{0.54}Al_{0.46}N$ multilayer film: (blue line) in the middle of the $Ti_{0.54}Al_{0.46}$ layer; (pink line) in the middle of the $Ti_{0.54}Al_{0.46}N$ layer.

The spectrum recorded from the middle of the nitride layer of the multilayer (Fig. 10b, pink line) resembles that of $Ti_{0.54}Al_{0.46}N$, but surprisingly the H peak is less intense and the second bump is shifted towards the low energies, which suggests that more N atoms are in four-fold environment. They are probably located in the disordered area since X-ray and electron diffraction patterns do not reveal the presence of wurtzite-like crystallized domains. In contrast, the spectrum recorded in the middle of the metallic layer looks like that of TiN and is typical of an octahedral nitrogen environment: the N atoms present in the metallic area are unambiguously in NTi_6 nano-grains.

V. Discussion

Multilayer coatings prepared with thin layers are more difficult to characterize than single-layer films due to interface phenomena. XRD was used to obtain information about the layer interface quality and to determine the period leading to the formation of a superlattice structure. For Λ = 10 nm, a superlattice structure was obtained and TEM provided images of the layered structure of this multilayer film. Then EELS was employed because it is an excellent technique for

investigating the nitrogen bonding in the metallic layer.

The lattice parameters of stress free $Ti_{0.54}Al_{0.46}$ and $Ti_{0.54}Al_{0.46}N$ layers are close to 4 Å (~ 4.0 for $Ti_{0.54}Al_{0.46}$ and ~ 4.2 Å for $Ti_{0.54}Al_{0.46}N$) and both grow along the [111] direction. Therefore, the period of $\Lambda = 10$ nm is a little more than twenty times the lattice parameters. Due to the interfacial roughness, it is not surprising that nitrogen atoms are present within the metallic part of the multilayer.

The N K-edge ELNES gives valuable information on the bonding of nitrogen atoms depending on their position along the growth direction. The relative position and intensity of the peaks are closely related to the nature of their nearest metallic neighbours. In $Ti_{0.54}Al_{0.46}N$ films (Fig. 10a) and in the middle of the $Ti_{0.54}Al_{0.46}N$ component of the multilayer (Fig. 10b), most of the nitrogen atoms are in six-fold coordination as in fcc TiN, but some of those in nano-grains with less metallic neighbours are in distorted hcp symmetry. The early TEM investigations of TiAlN films have indicated the presence of AlN precipitates around crystallized fcc columns [3,4]. The situation is more complex, and given the examination of the ELNES spectra, such precipitates are more likely either $NTiAl_3$ or NTi_2Al_2. Otherwise, in the middle of $Ti_{0.54}Al_{0.46}$ component layers deposited after stopping the nitrogen gas flow in the deposition chamber, the ELNES spectrum of Fig. 10b looks like the TiN one. All the nitrogen atoms located in the middle of the metallic layer are obviously surrounded by Ti atoms in six-fold coordination, that is, in fcc local symmetry. In conclusion, ELNES shows that there is a progressive evolution of the structure of the nitride nano-grains included in the metallic layer along the growth direction and they gradually acquire a TiN-like structure.

As far as the mechanical properties determined by nano-indentation tests are concerned, for $4 \leq \Lambda \leq 50$ nm, at h = 0, the indentation modulus of the multilayers is in the range of 340 ± 16 GPa $< M < 525 \pm 26$ GPa and follows a Hall and Petch evolution. Moreover, for $\Lambda = 4$ nm, the indentation modulus is very close to that of the nitride film: $M_{<200>c}$ ($Ti_{0.54}Al_{0.46}N$) = 512 ± 25

GPa. The XRD pattern, which presents a well-defined peak attributed to the $[200]_c$ direction of the $Ti_{0.54}Al_{0.46}N$ nitride, is consistent with this observation. ELNES shows that nitrogen atoms are present in the metallic component of the multilayer of period Λ = 10 nm, so nitrogen also diffuses in metallic layers of a 4-nm-period multilayer film. In the opposite case, for Λ = 50 nm and h = 0, the indentation modulus value, M = 340 $\pm$ 17 GPa, is close to that calculated from the mixture law, M = (M(TiAlN) + M(TiAl))/2 = 362 GPa. As above, this is confirmed by the XRD pattern, which shows two distinct and well-defined peaks attributed to the [111] directions of the nitride and metallic component layers. Note that, from an elastic point of view, fcc TiAlN is quasi-isotropic [7,57], which is not totally true for tetragonal TiAl.

For $4 \leq \Lambda \leq 50$, the hardness is in the range of 25 $\pm$ 2 GPa to 50 $\pm$ 4 GPa. A variety of mechanisms have been suggested to describe the hardening phenomena observed in nanoscale multi-layered superlattice coatings. The impediment of dislocation motion due to the difference in the shear moduli of the component layers, the coherency strain energy caused by lattice mismatch, and the variation of the interface width due to intermixing during deposition are the main examples of these mechanisms. Presently, as shown in Fig. 4b, the hardness evolution shows a good agreement with the Hall and Petch relationship, which indicates that dislocation pile-up is certainly the major strengthening mechanism [32,50]. Indeed, when the difference in shear moduli is high, which is certainly the case according to the indentation moduli values determined in this study, the force needed to move the dislocations across the boundary between the layers will be high and the hardness will increase as the superlattice period increases. But from a critical period Λ_d, it will be easier to move the dislocations within a layer than to move them across the boundary. Consequently, the force required to move the dislocations inside a layer decreases as the period increases. The critical period between these two regimes (breakdown in the Hall and Petch relationship) has been reported as Λ_d = 3.6 nm for TiN/NbN, Λ_d = 9.6 nm for TiAlN/TiN [48], and $2.4 < \Lambda_d < 4$ nm for $Ti_{1-x}Al_xN$/CrN for $0.23 < x < 0.72$

[50]. Presently, this transition has not been observed and certainly occurs at $\Lambda_d < 4$ nm in the $Ti_{0.54}Al_{0.46}/Ti_{0.54}Al_{0.46}N$ multilayer. The difference in the lattice parameters derived from the positions of the peaks in Fig. 1 is small. Consequently, the coherency strain effects do not significantly contribute to the hardening phenomena. However, as shown above (ELNES), due to a progressive evolution of the structure of the nitride nano-grains included in the $Ti_{0.54}Al_{0.46}$ metallic layers, the interfaces have nonzero width. The ratio between the interface width and the period decreases when the period increases. This could also contribute to the decrease in hardness when the period increases. Note that, whatever the period, $4 \leq \Lambda \leq 50$ nm, and for h = 0, the hardness is always greater than the one given by the mixture law, $H_B = 23$ GPa. Moreover, as for the indentation modulus, for $\Lambda = 50$ nm, the hardness value, $H_B = 25 \pm 2$ GPa, is fairly close to that predicted by the mixture law. A superlattice effect, $H_B > H_B(Ti_{0.54}Al_{0.46}N)$, is observed for the multilayer periods of $\Lambda = 4$, 10 (whatever the thickness), and 16 nm.

VI. Conclusion

In this paper, metallic/nitride ($Ti_{0.54}Al_{0.46}/Ti_{0.54}Al_{0.46}N$) multilayer films with different periods Λ ($4 < \Lambda < 50$ nm) were deposited from one TiAl target and one reactive gas N_2 using pulsed nitrogen flow.

The Hall and Petch effect was used to explain the enhancement of the hardness in the multilayers as a function of the period ($H_B \alpha 1/\sqrt{\Lambda}$) and a superlattice effect was obtained for multilayer coatings prepared with very thin component layers, that is, with periods in the range of 4 to 16 nm. Hence, for these multilayers, we obtained $H_B > H_B(Ti_{0.54}Al_{0.46}N) = 33$ GPa, and all of the hardness values are greater than the one given by the mixture rule.

The indentation moduli also present the same kind of evolution ($M_{<hkl>} \alpha 1/\sqrt{\Lambda}$) and are in the range of 340 GPa < M < 525 GPa ≈ M($Ti_{0.54}Al_{0.46}N$). Moreover, as for the hardness, when $\Lambda \leq$ 24 nm, the modulus values are higher than the one calculated with the mixture law.

For these different periods, due to the important interfacial roughness, nitrogen atoms are present within the metallic part of the multilayer. The analysis of nitrogen bonding within the two components of the $Ti_{0.54}Al_{0.46}N/Ti_{0.54}Al_{0.46}$ multilayer of period $\Lambda = 10$ nm reveals a progressive evolution of the structure of the nitride nano-grains.

In the nitride part, $Ti_{0.54}Al_{0.46}N$, of the multilayer, most of the nitrogen atoms are in a cubic-like environment as in TiN and some of them are in nano-grains with less metallic neighbours. In $Ti_{0.54}Al_{0.46}$ metallic layers, all the nitrogen atoms located in the middle of the layer are surrounded by Ti atoms in six-fold coordination, that is, in fcc local symmetry. Therefore, although some hexagonal AlN-like nano-grains probably remain in the grain boundaries of the nitride layers, the fcc TiN-like structure is predominant, which benefits the mechanical properties. In conclusion, this PVD reactive nitrogen pulsing process opens new directions in the deposition of structural coatings from one TiAl alloy target. It allows the deposition of multilayers with a superlattice structure exhibiting both better elastic modulus and higher hardness.

References

[1] W.D. Münz, Titanium aluminum nitride films: A new alternative to TiN coatings, Journal of Vacuum Science & Technology A, 4 (1986) 2717-2725.

[2] S.K. Khrais, Y.J. Lin, Wear mechanisms and tool performance of TiAlN PVD coated inserts during machining of AISI 4140 steel, Wear, 262 (2007) 64-69.

[3] K. Kutschej, P.H. Mayrhofer, M. Kathrein, P. Polcik, R. Tessadri, C. Mitterer, Structure, mechanical and tribological properties of sputtered $Ti_{1-x}Al_xN$ coatings with $0.5<x<0.75$, Surface and Coatings Technology, 200 (2005) 2358-2365.

[4] U. Wahlström, L. Hultman, J.E. Sundgren, F. Adibi, I. Petrov, J.E. Greene, Crystal growth and microstructure of polycrystalline $Ti_{1-x}Al_xN$ alloy films deposited by ultra-high-vacuum dual-target magnetron sputtering, Thin Solid Films, 235 (1993) 62-70.

[5] H.W. Hugosson, H. HÖgberg, M. Algren, M. Rodmar, T.I. Selinder, Theory of the effects of substitutions on the phase stabilities of $Ti_{1-x}Al_xN$, Journal of Applied Physics, 93 (2003) 4505-4511.

[6] A. Kimura, H. Hasegawa, K. Yamada, T. Suzuki, Effects of Al content on hardness, lattice parameter and microstructure of $Ti_{1-x}Al_xN$ films, Surface and Coatings Technology, 120–121 (1999) 438-441.

[7] M.J. Pac, S. Giljean, C. Rousselot, F. Richard, P. Delobelle, Microstructural and elasto-plastic material parameters identification by inverse finite elements method of $Ti_{(1-x)}Al_xN$ ($0 < x < 1$) sputtered thin films from Berkovich nano-indentation experiments, Thin Solid Films, 569 (2014) 81-92.

[8] H. Holleck, V. Schier, Multilayer PVD coatings for wear protection, Surface and Coatings Technology, 76–77 (1995) 328-336.

[9] W. Tillmann, E. Vogli, S. Momeni, Mechanical and tribological properties of Ti/TiAlN duplex coatings on high and low alloy tool steels, Vacuum, 84 (2009) 387-392.

[10] E. Vogli, W. Tillmann, U. Selvadurai-Lassl, G. Fischer, J. Herper, Influence of Ti/TiAlN-multilayer designs on their residual stresses and mechanical properties, Applied Surface Science, 257 (2011) 8550-8557.

[11] J.M. Castanho, M.T. Vieira, Effect of ductile layers in mechanical behaviour of TiAlN thin coatings, Journal of Materials Processing Technology, 143–144 (2003) 352-357.

[12] H. Meidia, A.G. Cullis, C. Schönjahn, W.D. Münz, J.M. Rodenburg, Investigation of intermixing in TiAlN/VN nanoscale multilayer coatings by energy-filtered TEM, Surface and Coatings Technology, 151–152 (2002) 209-213.

[13] J.S. Yoon, H.Y. Lee, J.G. Han, S.H. Yang, J. Musil, The effect of Al composition on the microstructure and mechanical properties of WC–TiAlN superhard composite coating, Surface and Coatings Technology, 142–144 (2001) 596-602.

[14] O. Ersen, M.-H. Tuilier, O. Thomas, P. Gergaud, P. Lagarde, Cubic local order around Al and intermixing in short-period AlN/TiN multilayers studied by Al K-edge extended x-ray absorption fine structure spectroscopy and x-ray diffraction, Applied Physics letters, 82 (2003) 3659-3661.

[15] O. Ersen, M.H. Tuilier, A. Thobor-Keck, C. Rousselot, R. Cortès, Relation between interfacial structure and mechanical properties in AlN/TiN bilayers investigated by EXAFS, Nuclear Instruments and Methods in Physics Research Section B: Beam Interactions with Materials and Atoms, 234 (2005) 308-320.

[16] C.J. Tavares, L. Rebouta, J.P. Rivière, T. Girardeau, P. Goudeau, E. Alves, N.P. Barradas, Atomic environment and interfacial structural order of TiAlN/Mo multilayers, Surface and Coatings Technology, 187 (2004) 393-398.

[17] Q. Luo, Z. Zhou, W.M. Rainforth, P.E. Hovsepian, TEM-EELS study of low-friction superlattice TiAlN/VN coating: the wear mechanisms, Tribology Letters, 24 (2006) 171-178.

[18] Y. Pinot, M.J. Pac, P. Henry, C. Rousselot, Y. Odarchenko, D.A. Ivanov, C. Ulhaq-Bouillet, O. Ersen, M.H. Tuilier, Friction behaviour of TiAlN films around cubic/hexagonal transition: A 2D grazing incidence X-ray diffraction and electron energy loss spectroscopy study, Thin Solid Films, 577 (2015) 74-81.

[19] N. Martin, J. Lintymer, F. Sthal, O. Banakh, H. Le Dréo, P.A. Steinman, M. Fenker, H. Kappl, C. Rousselot, C. Petitjean, M. Grafouté, A. Cavaleiro, N. Parreira, T. Polcar, P. Carvalho, F. Vaz, L. Rebouta, Procédé de pulvérisation réactive à signal de commande cyclique et dispositif correspondant, patent FR2905124, 2008.

[20] J.M. Chappé, N. Martin, J. Lintymer, F. Sthal, G. Terwagne, J. Takadoum, Titanium oxynitride thin films sputter deposited by the reactive gas pulsing process, Applied Surface Science, 253 (2007) 5312-5316.

[21] N. Martin, O. Banakh, A.M.E. Santo, S. Springer, R. Sanjinés, J. Takadoum, F. Lévy, Correlation between processing and properties of TiO_xN_y thin films sputter deposited by the reactive gas pulsing technique, Applied Surface Science, 185 (2001) 123-133.

[22] M. Grafouté, C. Petitjean, A. Diama, J.F. Pierson, J.M. Greneche, C. Rousselot, Structural investigations of iron oxynitride multilayered films obtained by reactive gas pulsing process, Surface and Coatings Technology, 272 (2015) 158-164.

[23] C. Petitjean, M. Grafouté, J.F. Pierson, C. Rousselot, O. Banakh, Structural, optical and electrical properties of reactively sputtered iron oxynitride films, Journal of Physics D: Applied Physics, 39 (2006) 1894-1898.

[24] C. Petitjean, M. Grafouté, C. Rousselot, J.F. Pierson, Reactive gas pulsing process: A method to extend the composition range in sputtered iron oxynitride films, Surface and Coatings Technology, 202 (2008) 4825-4829.

[25] M. Fenker, H. Kappl, O. Banakh, N. Martin, J.F. Pierson, Investigation of Niobium oxynitride thin films deposited by reactive magnetron sputtering, Surface and Coatings Technology, 201 (2006) 4152-4157.

[26] P. Carvalho, L. Cunha, E. Alves, N. Martin, E. Le Bourhis, F. Vaz, ZrO_xN_y decorative thin films prepared by the reactive gas pulsing process, Journal of Physics D: Applied Physics, 42 (2009) 195501.

[27] E. Aubry, S. Weber, A. Billard, N. Martin, Enhanced tunability of the composition in silicon oxynitride thin films by the reactive gas pulsing process, Applied Surface Science, 290 (2014) 148-153.

[28] A. Cacucci, V. Potin, L. Imhoff, M.C. Marco de Lucas, N. Martin, Structural analysis of W_3O/WO_3 and TiO/TiO_2 periodic multilayer thin films sputter deposited by the reactive gas pulsing process, Thin Solid Films, 520 (2012) 4778-4781.

[29] A. Cacucci, S. Loffredo, V. Potin, L. Imhoff, N. Martin, Interdependence of structural and electrical properties in tantalum/tantalum oxide multilayers, Surface and Coatings Technology, 227 (2013) 38-41.

[30] A. Cacucci, V. Potin, L. Imhoff, N. Martin, Structural and electrical properties in tungsten/tungsten oxide multilayers, Thin Solid Films, 553 (2014) 93-97.

[31] A. Zairi, C. Nouveau, A.B.C. Larbi, A. Iost, N. Martin, A. Besnard, Effect of RGPP process on properties of Cr-Si-N coatings, Surface Engineering, 30 (2014) 606-611.

[32] P.C. Yashar, W.D. Sproul, Nanometer scale multilayered hard coatings, Vacuum, 55 (1999) 179-190.

[33] M.-H. Tuilier, M.J. Pac, M. Gîrleanu, G. Covarel, G. Arnold, P. Louis, C. Rousselot, A.-M. Flank, Electronic and atomic structures of $Ti_{1-x}Al_xN$ thin films related to their damage behavior, Journal of Applied Physics, 103 (2008) 083524.

[34] E. Kusano, M. Kitagawa, H. Nanto, A. Kinbara, Hardness enhancement by compositionally modulated structure of Ti/TiN multilayer films, Journal of vacuum science and technology A, 16 (1998) 1272-1276.

[35] W.C. Oliver, G.M. Pharr, An improved technique for determining hardness and elastic modulus using load and displacement sensing indentation experiments, Journal of Materials Research, 7 (1992) 1564-1583.

[36] J.J. Vlassak, W.D. Nix, Measuring the elastic properties of anisotropic materials by means of indentation experiments, Journal of the Mechanics and Physics of Solids, 42 (1994) 1223-1245.

[37] S. Chen, L. Liu, T. Wang, Investigation of the mechanical properties of thin films by nanoindentation, considering the effects of thickness and different coating-substrate combinations, Surface and Coatings Technology, 191 (2005) 25-32.

[38] H. Gao, C.H. Chiu, J. Lee, Elastic contact versus indentation modeling of multi-layered materials, International Journal of Solids and Structures, 29 (1992) 2471-2492.

[39] R.B. King, Elastic analysis of some punch problems for a layered medium, International Journal of Solids and Structures, 23 (1987) 1657-1664.

[40] A.M. Korsunsky, M.R. McGurk, S.J. Bull, T.F. Page, On the hardness of coated systems, Surface and Coatings Technology, 99 (1998) 171-183.

[41] J. Mencik, D. Munz, E. Quandt, E.R. Weppelmann, M.V. Swain, Determination of elastic modulus of thin layers using nanoindentation, Journal of Materials Research, 12 (1997) 2475-2484.

[42] A. Perriot, E. Barthel, Elastic contact to a coated half-space: Effective elastic modulus and real penetration, Journal of Materials Research, 19 (2004) 600-608.

[43] M. Zhou, Y. Makino, M. Nose, K. Nogi, Phase transition and properties of Ti-Al-N thin films prepared by r.f.-plasma assisted magnetron sputtering, Thin Solid Films, 339 (1999) 203-208.

[44] A. Horling, L. Hultman, M. Oden, J. Sjolen, L. Karlsson, Mechanical properties and machining performance of $Ti_{1-x}Al_xN$-coated cutting tools, Surface and Coatings Technology, 191 (2005) 384-392.

[45] M. Chinmulgund, R.B. Inturi, J.A. Barnard, Effect of Ar gas pressure on growth, structure, and mechanical properties of sputtered Ti, Al, TiAl, and Ti3Al films, Thin Solid Films, 270 (1995) 260-263.

[46] M.S. Bobji, S.K. Biswas, Hardness of a surface containing uniformly spaced pyramidal asperities, Tribology Letters, 7 (1999) 51-56.

[47] M. Qasmi, P. Delobelle, Influence of the average roughness Rms on the precision of the Young's modulus and hardness determination using nanoindentation technique with a Berkovich indenter, Surface and Coatings Technology, 201 (2006) 1191-1199.

[48] H.C. Barshilia, K.S. Rajam, A. Jain, K. Gopinadhan, S. Chaudhary, A comparative study on the structure and properties of nanolayered TiN/NbN and TiAlN/TiN multilayer coatings prepared by reactive direct current magnetron sputtering, Thin Solid Films, 503 (2006) 158-166.

[49] B.C. Kang, H.Y. Kim, O.Y. Kwon, S.H. Hong, Bilayer thickness effects on nanoindentation behavior of Ag/Ni multilayers, Scripta Materialia, 57 (2007) 703-706.

[50] J.K. Park, H.J. Park, J.H. Ahn, Y.J. Baik, Effect of Ti to Al ratio on the crystalline structure and hardening of a $Ti_{1-x}Al_xN$/CrN nanoscale multilayered coating, Surface and Coatings Technology, 203 (2009) 3099-3103.

[51] A.K. Bhattacharya, W.D. Nix, Analysis of elastic and plastic deformation associated with indentation testing of thin films on substrates, International Journal of Solids and Structures, 24 (1988) 1287-1298.

[52] T.Y. Tsui, G.M. Pharr, W.C. Oliver, C.S. Bhatia, R.L. White, S. Anders, A. Anders, I.G. Brown, Nanoindentation and Nanoscratching of Hard Carbon Coatings for Magnetic Disks, Material Research Society Proceedings, 383 (1995) 447-452.

[53] M. Gîrleanu, M.J. Pac, P. Louis, O. Ersen, J. Werckmann, C. Rousselot, M.-H. Tuilier, Characterisation of nano-structured titanium and aluminium nitride coatings by indentation, transmission electron microscopy and electron energy loss spectroscopy, Thin Solid Films, 519 (2011) 6190-6195.

[54] R. Gago, A. Redondo-Cubero, J.L. Endrino, I. Jiménez, N. Shevchenko, Aluminum incorporation in $Ti_{1-x}Al_xN$ films studied by x-ray absorption near-edge structure, Journal of Applied Physics, 105 (2009) 113521.

[55] R. Gago, F. Soldera, R. Hübner, J. Lehmann, F. Munnik, L. Vàzquez, A. Redondo-Cubero, J.L. Endrino, X-ray absorption near-edge structure of hexagonal ternary phases in sputter-deposited TiAlN films, Journal of Alloys and Compounds, 561 (2013) 87-94.

[56] D. Holec, R. Rachbauer, D. Kiener, P.D. Cherns, P.M.F.J. Costa, C. McAleese, P.H. Mayrhofer, C.J. Humphreys, Towards predictive modeling of near-edge structures in electron energy-loss spectra of AlN-based ternary alloys, Physical Review B, 83 (2011) 165122.

[57] Y. Yang, H. Lu, C. Yu, J.M. Chen, First-principles calculations of mechanical properties of TiC and TiN, Journal of Alloys and Compounds, 485 (2009) 542-547.